Originally published as:

Correlation between deep fluids, tremor and creep along the central San Andreas Fault

Michael Becken[1,2,*], Oliver Ritter[1], Paul A. Bedrosian[3], Ute Weckmann[1,2]

1. GFZ German Research Centre for Geosciences, Telegrafenberg, 14473 Potsdam, Germany

2. University Potsdam, Institute of Geosciences, Karl-Liebknecht-Str. 24, 14476 Potsdam-Golm, Germany

3. US Geological Survey, MS 964, Box 25046, Bldg 20, Denver, CO 80225 USA

* now at: Westfälische Wilhelms Universität Münster, Institute of Geophysics, Corrensstr. 24, 48149 Münster, Germany

The seismicity pattern along the San Andreas Fault (SAF) near Parkfield and Cholame, California, varies distinctly over a length of only 50 km. Within the brittle crust, the presence of frictionally weak minerals, fault-weakening high fluid pressures or chemical weakening are considered possible explanations for an anomalously weak fault northwest of Parkfield[1-4]. Non-volcanic tremor from lower-crustal and upper-mantle depths[5-7] is most active ~30 km to the southeast of Parkfield and is thought to be associated with high pore-fluid pressures at depth[8]. Here, we present geophysical evidence of fluids migrating into the creeping section of the SAF that appear to originate from the same source region in the uppermost mantle that stimulates tremor, and that along-strike variations in tremor activity and amplitude are related to strength variations in the lower crust and upper mantle. Interconnected fluids can explain a deep zone of anomalously low electrical resistivity which has been imaged by magnetotelluric data to the southwest of the Parkfield-Cholame segment. Near Cholame, where fluids appear trapped below a resistive cap, tremor concentrates adjacent to the inferred fluids within a mechanically strong zone of high resistivity. In stark contrast, sub-vertical zones of low resistivity breach the entire crust near the San Andreas Fault Observatory at Depth (SAFOD) drilling northwest of Parkfield and imply pathways for deep fluids into the

eastern fault block, coincident with a mechanically weak crust and the lower tremor amplitudes in the lower crust. Fluid influx into the fault system is consistent with hypotheses of fault-weakening high fluid pressures in the brittle crust.

Magnetotelluric data sense the electrical resistivity of the Earth, a physical parameter particularly sensitive to the presence of low resistivity phases such as aqueous fluids, partial melts or metallic compounds. Fluid phases have electrical resistivities orders of magnitude lower than the rock matrix, and thus relatively small amount of fluids, when interconnected, can decrease bulk rock resistivity by several orders of magnitude[9]. Fluids additionally have a significant weakening effect on the rheology of rocks, even more so if fluids form an interconnected network[10]. Measurements of electrical resistivity can therefore be used to constrain the volume of subsurface fluids, their interconnectivity, and the rheology of the crust and mantle.

We collected magnetotelluric data along seven profiles across the SAF near Parkfield and Cholame, covering the tremor concentration zone near Cholame and the transition from locked to creeping behaviour (Fig. 1a). The most prominent structure revealed by the MT data is a deep low-resistivity zone (1-5 ohm-m) centred 30-40 km southwest of the SAF below 15-20 km depth (Fig. 1b). This anomaly occupies a broad region in the lower crust and upper mantle between the surface traces of the Rinconada fault, a former strand of the SAF, and the modern-day SAF. Along profiles 4-7, which cross the SAF at the tremor concentration zone near the northern end of the locked segment[5,7], crustal resistivities are in excess of 500 ohm-m for the Pacific plate, in contrast to the moderately resistive crustal formations (10 -100 ohm-m) of the North American plate. These values are typical for the granitic rocks of the Salinian Block and for the metamorphic and sedimentary sequences contained within the Franciscan formation, respectively. The subduction complex constituting the Franciscan formation includes a great variety of lithologies, including fragments of

oceanic crust, bodies of greenstones and other metamorphic and volcanic rocks. Along-strike variations in the resistivity structure of the Franciscan, such as the high resistivities to the northeast of the SAF near Parkfield (profiles 2 and 3, Fig. 1b), reflect this heterogeneity.

The SAF itself appears most prominently beneath the Cholame Valley (profile 5, Fig. 2b) as a vertical resistivity contrast extending below the brittle-ductile transition to depths of 20 km or more. Transitioning to the northwest, where the SAF exhibits creep and microseismicity, profiles 1-3 image a low resistivity (5-30 ohm-m) linkage between the deep low resistivity zone to the southwest and the SAF to the northeast, in marked contrast to the resistivity models farther south.

The anomalously low electrical resistivity in the lower crust and upper mantle provides geophysical evidence for a deeply seated fluid source offset to the southwest of the SAF. Low electrical resistivity has been reported at similar depths along numerous active margins, including the Pacific-Australian Plate collision zone in New Zealand[11], beneath the Tibetan plateau[12], and the Altiplano plateau of the Andes in Chile and Bolivia[13]. Explanations involved the presence of partial melt[14] in combination with aqueous fluids, imply a weakened rheology, and support models of lower-crustal flow[12]. Modelling of the Coast Range heat flow anomaly suggests temperatures of ~800°C at 30 km depth near Parkfield[15] - too cold for a partially molten upper mantle. The resistivity of aqueous fluids depends strongly on temperature and salinity. The salinity of sea water is a conservative assumption for the fluid phase. At 800°C the electrical resistivity of sea water is 0.03 ohm-m, approximately ten times lower than at room temperatures[16]. The Hashin-Shtrickman upper bound[17] for a two-phase system composed of a resistive rock matrix (100 ohm-m) and a low resistivity aqueous fluid phase (0.03 ohm-m) requires 3 vol.% of perfectly interconnected porosity over

a large volume to explain bulk resistivities of 1 ohm-m; higher fluid salinities would require less interconnection and/or lower porosity.

Aqueous fluid networks can explain the observed low resistivities, but not unambiguously. A region in the crust weakened by shearing and faulting can become mineralized by chemical precipitation reactions[18,19]. Continued shearing deformation can further increase the interconnectivity of such mineralized zones and result in low electrical resistivities[20]. However, independent geophysical observations strongly support our preferred interpretation of a deep fluid source. A seismic refraction profile approximately coincident with profile 5 reveals a low velocity zone with compressional wave-speeds of less than 5 km/s at 15-22 km depth[21], coincident with the top of the low-resistivity zone and consistent with the presence of fluids in this region (Fig. 2b).

Fluids in this depth range are also likely involved in the generation of deep non-volcanic tremor along this fault segment[6,8]. Teleseismic and tidal triggering of tremor episodes at the SAF indicate that tremor nucleates in regions close to mechanical failure at near-lithostatic fluid pressures[8]. For the magnetotelluric profiles 5-7 across the tremor concentration zone near Cholame, the inversion reveals a deep low resistivity region which is bounded from above and laterally by resistive formations (Figs. 1b, 2b). Here, the tremor source region appears to coincide with the high resistivity rocks, adjacent to the less resistive and potential fluid source area. Inversions of the MT data confirm the resistive cap as a very robust feature of the models. Any low resistivity connection into the upper crust (as observed northeast of Parkfield) results in a significant increase of data misfit (see supplementary information).

Tremor near Cholame separates spatially into a southwestern zone with periodic tremor episodes and a northeastern zone with aperiodic episodes[7]. Our resistivity models suggest that the fluid source (i.e. low resistivity) is located to the southwest of the periodic tremor zone. Ongoing fluid generation by mantle dehydration reactions[4] could result in high fluid pressures in the low resistivity zone, and consequently, in fluids continuously driven through fracture systems towards and into the more resistive tremor regions. Observations of high seismic reflectivity[21] (cf. Fig. 2b) at tremor source depths between the low resistivity fluid source and the more resistive tremor zone are consistent with deformed and fractured material. Lateral migration of fluids could be responsible for elevated fluid pressures in the tremor source region[8]. The periodic tremor episode occurrences are located closer to the fluid source and could reflect a failure mechanism involving cyclic fluid pressure accumulation and release.

A similar fluid-triggering scenario has been suggested to account for the globally observed correlation between electrical resistivity and brittle failure in the upper crust[22], including along the SAF[23]. Brittle rock failure and earthquakes often occur close to the boundary or within electrically resistive regions but adjacent to zones of lower resistivity[22]. These observations have been explained with migration of fluids from a permeable, mechanically weak source into a less permeable, mechanically strong, and electrically resistive region. This transport can induce high fluid pressures and rock failure within the resistive region, depending on the concentration of stress and the penetration depth of fluids into the rocks. Hydrofracturing or reaction-enhanced permeability[24] can be efficient mechanisms to facilitate fluid flow within low-permeability rocks under high confining pressures persisting in the lower crust and upper mantle.

Tremor amplitudes along the central SAF vary by a factor of seven[6] and correlate with variations of resistivity by a factor of 100 between Cholame and northwest of Parkfield (Fig. 3). High amplitude tremors

appear to originate predominantly from the resistive lower crustal formations beneath Cholame (Fig. 3a), whereas the less resistive regions northwest of Parkfield exhibit low tremor amplitudes or are devoid of measurable tremor. Deformation at lower crustal depth is generally ductile. However, high fluid pressures can facilitate brittle failure also within an otherwise ductile deformation regime[6,8]. Under these circumstances, brittle failure rather than ductile deformation has been considered an appropriate model for tremor[8], and tremor amplitude may be a key to illuminate the physical conditions within the source region. The apparent systematic spatial variations of tremor activity and amplitudes and electrical resistivity along the deep central SAF[6] (Fig. 3b) likely reflect variable conditions for brittle failure and indicate changes of mechanical properties and hydraulic conditions along the deep extension of the fault zone. The correspondence between resistivity and tremor amplitude leads us to conjecture that strength controls tremor amplitudes. Figure 3c depicts electrical resistance, here defined as the inverse of the depth-integrated reciprocal resistivity, as a qualitative measure of the mechanical strength of the tremor zone. The resistivity models and the variations of lower crustal resistance argue for mechanically stronger rocks in the resistive tremor concentration zone beneath Cholame as opposed to mechanically weaker material in the less resistive lower crust northeast of Parkfield. Weak lower crustal material near SAFOD is also consistent with an anisotropic low-velocity, high compressional-to-shear-wave ratio layer at 20 to 25 km depth, inferred from receiver functions and interpreted as a sliver of serpentinite[25].

The weakness of the low resistivity lower crust near SAFOD can be explained with a fluid-filled porosity network. Our resistivity models show that the deep fluid source is offset from the SAF to the southwest and located beneath the Pacific plate. From here, low resistivity fluid pathways breach the lower crust near SAFOD and open out into an upper crustal wedge of low electrical resistivity between the seismically-

defined SAF to the southwest and the Waltham Canyon Fault to the northeast[26]. This crustal zone of low resistivity is less pronounced at profile 1, and it is unknown if it extends along the creeping segment.

Fluid ascent across the Pacific – North American Plate boundary into the fault-adjacent country rock of the North-American plate can contribute to super-hydrostatic fluid pressures along the creeping section of the SAF. Support for the existence of a connection to the lower crust and upper mantle comes from elevated mantle-derived gas concentrations found at SAFOD[27] and in nearby water-wells penetrating the eastern fault block. Mantle-derived fluids contributing to fault-weakening high fluid pressures[4] are considered one explanation for the frictional weakness of the SAF northeast of Parkfield. However, the role fluids play in the mechanics of this fault segment is still debated, because SAFOD observations did not provide evidence for elevated pore pressures directly within the actively deforming fault strands at the depth where the borehole intersects the fault[28].

MT cannot provide unique answers about the nature of the fluid source in the lower crust and upper mantle. It has been suggested that fluids are released from ongoing dehydration of serpentinised mantle wedge material[4], a relic of former subduction along coastal California. Such dehydration can last for tens of millions of years[4] and can be responsible for high fluid pressures in the tremor source region and ultimately, the supply of fluids into the crust near SAFOD. We speculate that crustal pathways for fluids near SAFOD reflect zones of intensively deformed material which coincide with fault-related exhumation of serpentinite to shallower crustal levels. Fluid release from lower crustal and upper mantle formations can (1) cause higher fluid pressures at shallower levels and result in mechanical weakening of the seismogenic SAF and the fault-adjacent country rocks of the North American Plate (2) support fluid-assisted chemical weakening (3) and increase chemical reaction rates. To the southeast, where fluids are trapped beneath an

impermeable cap in the crust, the fault is in a transitional-to-locked state. High pore pressures within the mantle and lower crust, accompanied by episodic fluid redistribution and seismic energy release appear to be responsible for the generation of tremor. Along the central SAF, the source for fluids migrating into the creeping section and stimulating the tremor region is offset to the southwest of the surface trace of the SAF. Tremor amplitude variations along the deep extension of the SAF appear to reflect fluid-controlled strength variations.

Methods Summary:

The Magnetotelluric method uses natural electromagnetic field variations to probe the electrical resistivity structure of the Earth's interior. For this study, MT data were collected in a series of field experiments between 2005 and 2008 with up to 45 simultaneously recording instruments. Robust remote and multi-remote reference processing was used to estimate MT transfer functions. The data were inverted into electrical resistivity, using a regularized two-dimensional (2D) non-linear conjugate gradient approach[30]. Regularization of the model is necessary because MT utilizes the diffusion of low-frequency natural electromagnetic fields within the conducting earth, which poses a mathematically ill-posed, under-determined inverse problem. The inversion minimizes a Tikhonov regularized functional as a trade-off between a structure penalty functional and the data residual norm weighted with the data variances. The structure penalty is a weighted integral of the Laplacian squared of the logarithmic model. Weights have been defined to generate increasing horizontal and vertical smoothing with increasing depth. 2D inversion assumes that resistivity is constant along strike. This assumption is not strictly satisfied given the partly 3D characteristics of the MT data. However, the predominant MT impedance strike directions determined from tensor decomposition[29] are consistent with a predominant geological strike which parallels the SAF in the

area. A down-weighting scheme was applied to data with 3D effects in order to reduce bias in the 2D inversion[26].

References:

1. Moore, D. E. & Rymer, M. J. Talc-bearing serpentinite and the creeping section of the San Andreas fault. *Nature* **448**, 795-797 (2007).

2. Holdsworth, R. E. et al. Fault rocks from the SAFOD core samples: Implications for weakening at shallow depths along the San Andreas Fault, California. *J. Struct. Geol.* **33**, 132-144 (2011).

3. Lockner, D. A., Morrow, C., Moore, D. & Hickman, S. Low strength of deep San Andreas fault gouge from SAFOD core. *Nature* **472**, 82-85 (2011).

4. Fulton, P. M. & Saffer, D. M. Potential role of mantle-derived fluids in weakening the San Andreas Fault. *J. Geophys. Res.* **114**, B07408 (2009).

5. Nadeau, R. M. & Dolenc, D. Nonvolcanic tremors deep beneath the San Andreas Fault. *Science* **21**, 389 (2005).

6. Shelly, D. R. & Hardebeck, J. L. Precise tremor source locations and amplitude variations along the lower-crustal central San Andreas Fault, *Geophys. Res. Let.* **37**, L14301 (2010).

7. Zhang, H., Nadeau, R. M., & Toksoz, M. N. Locating non-volcanic tremors beneath the San Andreas Fault using a station-pair double-difference location method, *Geophys. Res. Lett.* **37**, L13304 (2010).

8. Thomas, A. M., Nadeau, R. M. & Bürgmann, R. Tremor-tide correlations and near-lithostatic pore pressure on the deep San Andreas fault, *Nature* **462**, 1048-1051 (2009).

9. Guenguen, V. & Palciauskas, Y. *Introduction to the Physics of Rocks*. Princeton University Press, UK, (1994).

10. Bürgmann, R. & Dresen, G. Rheology of the Lower Crust and Upper Mantle: Evidence from Rock Mechanics, Geodesy, and Field Observations. *Annu. Rev. Earth Planet. Sci.*, **36**, 531–67 (2008).

11. Wannamaker, P. E. et al. Fluid and deformation regime of an advancing subduction zone at Marlborough, New Zealand. *Nature* **460**, 733-736 (2010).

12. Unsworth, M., et al. Crustal rheology of the Himalaya and Southern Tibet inferred from magnetotelluric data. *Nature* **438**, 78-81 (2005).

13. Brasse, H., et al. The Bolivian Altiplano conductivity anomaly. *J. Geophys. Res.* **107** doi:10.1029/2001JB000391 (2002).

14. Schilling, F. R. & Partzsch, G. M. Quantifying partial melt fraction in the crust beneath the central Andes and the Tibetan plateau. *Phys. Chem. Earth* **26**, 239-246 (2001).

15. Sass, J. H., et al. Thermal regime of the San Andreas Fault near Parkfield, California. *J. Geophys. Res.* **102**, 27.575-27.585 (1997).

16. Quist, A. S. & Marschall, W. L. Electrical conductances of aqueous sodium chloride solutions from 0 to 800° and at pressures to 4000 bars. *J. Phys. Chem.* **72**, 684-703 (1968).

17. Hashin, Z. & Shtrikman, S. A variational approach to the theory of effective magnetic permeability of multiphase materials. *J. Appl. Phys.* **33**, 3125–3131 (1962).

18. Weckmann, U., Ritter, O. & Haak, V. A magnetotelluric study of the Damara Belt in Namibia: 2. MT phases over 90° reveal the internal structure of the Waterberg Fault/Omaruru Lineament. *Physics of the Earth and Planetary Interiors*, **138**, 91-112 (2003).

19. Ritter, O., et al. Electrical conductivity images of active and fossil fault zones, in: Bruhn, D. and Burlini, L. (eds.) High-Strain Zones: Structure and Physical Properties, Geological Society of London Special Publications, **245**, 165-186 (2005).

20. Ritter, O. et al. Very high electrical conductivity beneath the Münchberg Gneiss area in Southern Germany: implications for horizontal transport along shear planes. *Geophys. J. Int.* **139**, 161-170 (1999).

21. Trehu, A. M. & Wheeler, W. H. Possible evidence for subducted sedimentary materials beneath central California. *Geology* **15**, 254-258 (1987).

22. Gürer, A. & Bayrak, M. Relation between electrical resistivity and earthquake generation in the crust of West Anatolia, Turkey. *Tectonophysics*, **445**, 49-65 (2007).

23. Bedrosian, P. A. et al. Geophysical images of the creeping segment of the San Andreas Fault: Implications for the role of crustal fluids in the earthquake process. *Tectonophysics* **385**, 137-158 (2004).

24. Tenthorey, E., & Stephen F. C. Reaction-enhanced permeability during serpentinite dehydration. *Geology* **31**, 921-924 (2003).

25. Ozacar, A. A. & Zandt, G. Crustal structure and seismic anisotropy near the San Andreas Fault at Parkfield, California. *Geophys. J. Int.* **178**, 1098-1104 (2009).

26. Becken, M. et al. A deep crustal fluid channel into the San Andreas Fault system near Parkfield, California. *Geophys. J. Int.* **173**, 718-732 (2008).

27. Wiersberg, T. & Erzinger, J. A helium isotope cross-section study through the San Andreas Fault at seismogenic depths, *Geochem. Geophys. Geosyst.*, **8**, (2007).

28. Zoback, M., Hickman, S. & Ellsworth, W. Scientific drilling into the San Andreas fault zone. *Eos Trans. AGU* **91,** 197–199 (2010).

29. Becken, M. & Burkhardt, H. An ellipticity criterion in magnetotelluric tensor analysis. *Geophys. J. Int.* **159**, 69-82 (2004).

30. Rodi, W. & Mackie, R. L. Nonlinear conjugate gradients algorithm for 2D magnetotelluric inversion.

Geophysics **66**, 174-187 (2001).

Author Contributions: All authors participated as responsible scientists in the various field experiments. M.B. processed the time series, analyzed and inverted the MT data and validated the resistivity models. All authors contributed to the interpretation and the manuscript. O. R. was PI of the DFG/GFZ funded research proposals.

Author Information: Reprints and permissions information is available at www.nature.com/reprints. The authors declare no competing financial interest. Correspondence and requests for materials should be addressed to M. B. (michael.becken@uni-muenster.de).
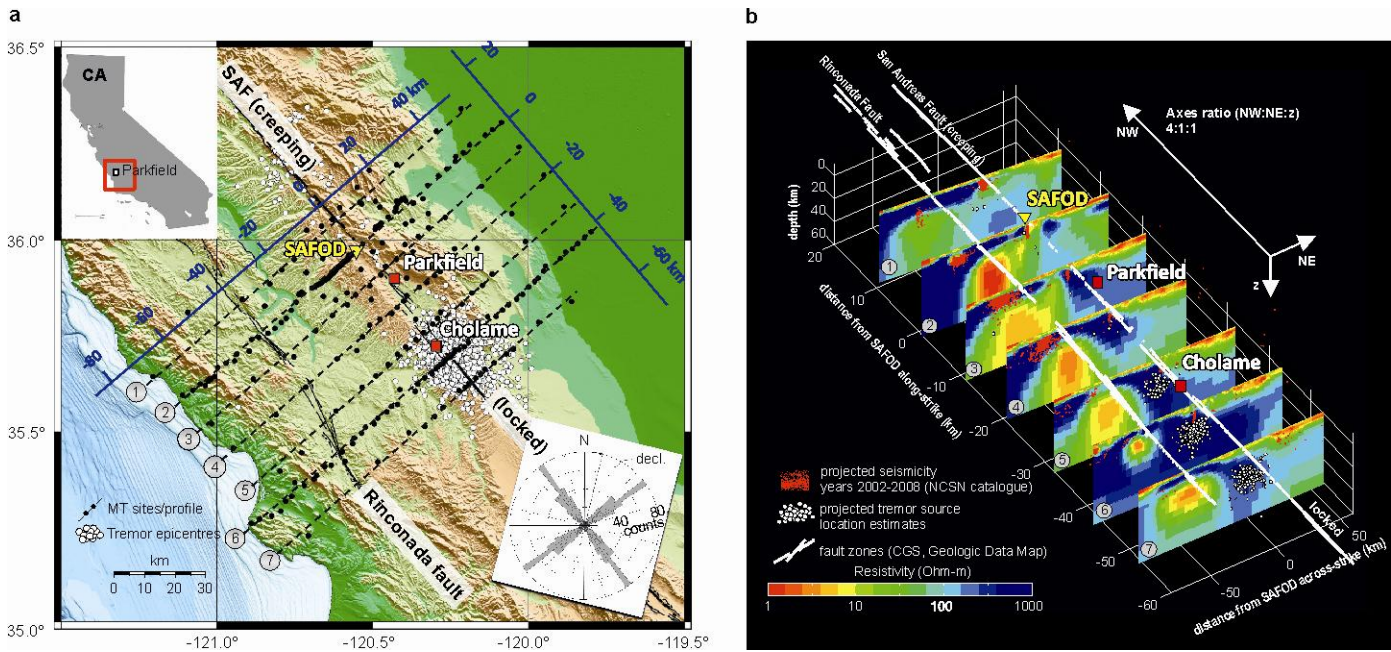
Figures

Figure 1 | **Magnetotelluric resistivity sections across the central San Andreas Fault. a,** Map view. Black dots show magnetotelluric stations along seven ~130 km-long profiles. MT tensor decomposition[29] yields geoelectric strike estimates (inset rose diagram), which are consistent with the orientation of the SAF. Creep rates of the SAF decay from ~30mm/yr northwest of SAFOD to less of 5 mm/yr southeast of Cholame[1]. White dots show tremor epicentres[7]. Figs. 1b, 2 and 3 use coordinates relative to SAFOD (blue axes). **b,** Electrical resistivity sections. Low resistivity in the lower crust and upper mantle is attributed to hot saline fluids. Fluid upwelling can occur into the creeping SAF near SAFOD. Near the locked segment, fluids appear trapped adjacent to the tremor concentration zone and restrained from escaping into the upper crustal portion of the SAF. Tremor sources[7] (white dots) and seismicity (red dots) are superimposed.
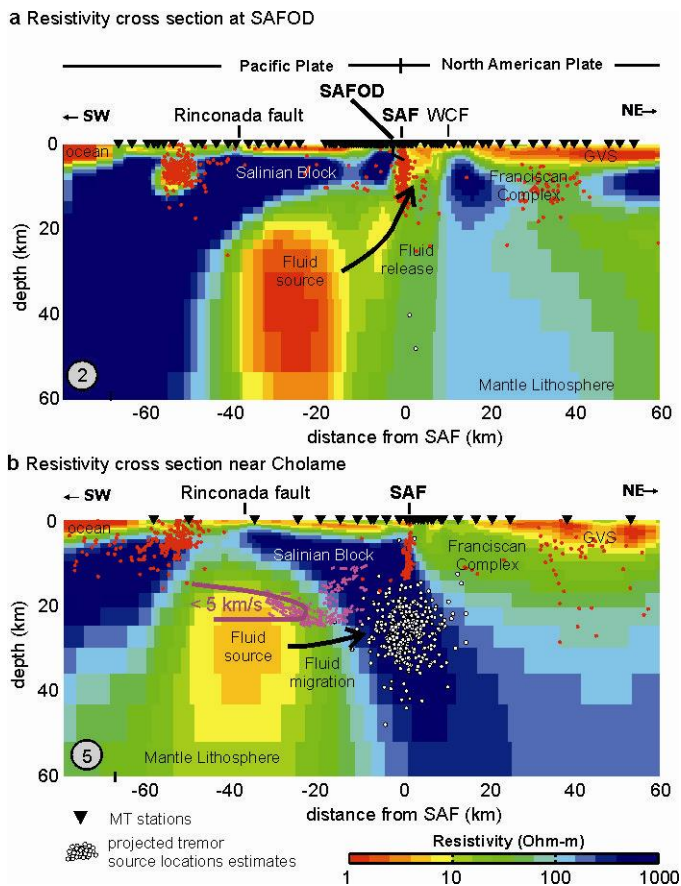
Figure 2 | Two distinct electrical resistivity models. **a,** Low electrical resistivity pathways for deep fluids breach the entire crust near SAFOD and provide a linkage (black arrow) between the fluid source beneath the Salinian Block on the Pacific side and the upper crust on the North American side of the fault. Fluid flow across the plate boundary likely occurs at the base of the crust below the seismically defined fault (red dots depict seismicity). **b,** Fluid pathways into the crust are absent for the Cholame segment of the fault. Here, the low resistivity fluid source is surrounded by highly resistive material and isolated from the SAF. Tremor (white dots) concentrates in the resistive zone[7]. A wedge-shaped low-velocity zone (thick purple line is the 5km/s seismic low-velocity contour interpreted from seismic refraction data[21]) coincides with the top of the low-resistivity fluid region. High seismic reflectivitiy (thin purple lines)[21] sandwiched between the low-resistivity/low-velocity zone and the tremor region indicates heterogeneous material, such as fracture or deformation zones which in turn can enable pathways for lateral fluid flow. WCF Waltham Canyon fault; GVS
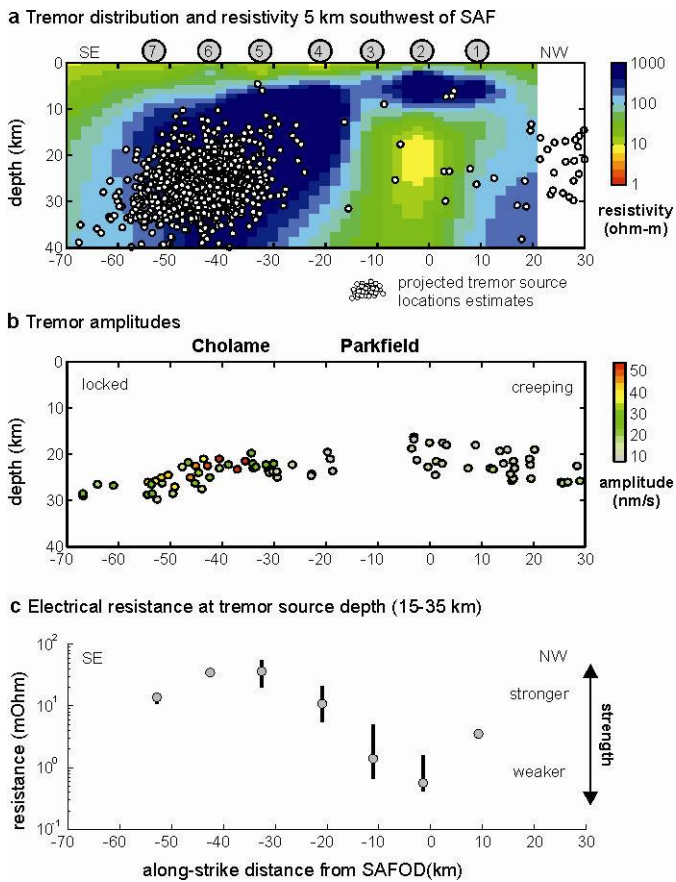
Great Valley Sequence.

Figure 3 | Relation between electrical resistivity and tremor. a) Tremors[7] projected onto a resistivity slice, which is interpolated from the 2D inversion models at -5 km distance from the SAF. **b)** Tremor amplitude estimates of individual tremor episodes[6]. **c)** Electrical resistance, the inverse of the depth-integrated reciprocal resistivity, computed for the tremor source depth range at -5 km distance; vertical bars indicate minimum and maximum resistances in the distance-range [-10 km, 0 km] along the individual profiles. Tremor concentrations and the largest tremor amplitudes correlate with the resistive regions. In contrast, zones exhibiting low tremor activity and low tremor amplitudes are associated with areas of low resistivity. We interpret electrical resistance in terms of mechanical strength to explain tremor amplitude variations along the SAF.

Methods

The 250 five-channel MT stations were recorded during three surveys in the years 2005, 2007 and 2008. All sites were equipped with induction coils magnetometers and non-polarisable electrodes (spanning orthogonal electric dipoles of ~60 m length) to measure the three components of the magnetic field and the horizontal electric field components. 3-4 days recording with this configuration yielded sufficient data to cover a broad-band period range of MT field variations from 0.01 s to more than 1000 s. In addition, 120 of the sites were equipped with fluxgate magnetometers and operated for 2 to 5 weeks to cover the long-period MT period range up to 20.000 s. Up to 45 simultaneously recording instruments were deployed, yielding great flexibility in subsequent remote-reference and multi-remote-reference processing of the data. In addition to our own measurements, we included some of the earlier MT data coincident with the central parts of profile 2 near SAFOD and profile 5 across the Cholame Valley[31,32].

The primary step in MT data analysis is to estimate the linear transfer functions between the horizontal electric and magnetic field components (impedance tensor **Z**) and between the vertical and horizontal magnetic field components (vertical magnetic transfer function **T**). MT transfer functions are diagnostic of subsurface electrical resistivity structure and are thus the quantities used for subsequent numerical resistivity model construction. Standard robust processing techniques in frequency domain[33-35] produced high-quality transfer functions for periods longer than 5 s, but often failed to separate the shorter-period MT signal from strong periodic noise with a fundamental period of ~5.1 s that was correlated over all channels and over wide areas. Noise levels were particularly high near buried gas pipelines suggesting cathodic protection currents commonly imposed on pipelines as the source of this noise. Remote reference techniques[33], multi-remote reference[36] as well as rejection of individual stacks based on phase constraints[35] could not significantly improve the short-period data quality. Instead, we pre-processed the time-series with a fractional delay filter that proved to be a powerful tool in

removing harmonic noise. The filter substracts a delayed version of the time series from itself, which causes destructive interference at the delay period and all harmonics. The delay period corresponds to the fundamental period of the harmonic noise signal. Because the fundamental noise period does not fit into our sampling schemes, the fractional delay filter is designed to perform a interpolation of the signal in order to compute the delayed signal. The interpolation can be made exact because the signal is bandlimited[37]. For subsequent remote-reference processing we applied the same delay filter also to the clean reference sites. With this processing we could significantly improve the data quality at short periods.

2D inversion techniques were applied to convert the estimated MT transfer functions to the resistivity models discussed in the main text. MT transfer functions inherently contain measures that can justify a 2D interpretation and that define the geo-electric strike direction to which the data must be rotated prior to model computation. We extracted these measures from the impedance data with decomposition methods that attempt to separate the regional 2D MT response from the so-called galvanic distortion effect of charge accumulations at near-surface resistivity heterogeneities[38]. We employed the impedance tensor decomposition technique described by Becken and Burkhardt[29] to analyze the distortion effect, the dimensionality of the data and, because we found conditions that generally justify a 2D interpretation, to estimate the rotation angle corresponding to the geo-electric strike direction. MT strike estimates, however, have an inherent ambiguity of 90°. Considering the orientations of the major structural trends in the area (the Coast line, the low resistivity sedimentary fill of the San Joaquin Valley, the SAF and associated geological units within the Coast Ranges), which are sub-parallel features elongated in the NW-SE direction, we constrained the strike estimates to the range 0°-90°W. We determined consistent multi-period strike estimates for each MT site separately, ranging between 35°W and 60°W, and a global strike estimate of 41°W using all available sites and periods jointly (inset in Figure 1a, main text). This geoelectric strike direction is in good agreement with dominant geological trends, particularly with the strike of the SAF in the segment under investigation. Nevertheless, variations of impedance phases oblique to strike are also visible, and indicate, in

conjunction with the off-profile orientation of induction vectors, the presence of 3D effects in some regions (see Figure S1).

In rotated coordinates, and in a true 2D environment with the x-axis oriented along-strike, the Zxy and Zyx impedance then correspond to the E- and B-Polarization impedances being associated with along-strike and across-strike currents, respectively. Along-strike current concentrations are also associated with a vertical magnetic field anomaly at the surface. For 2D model construction, we included the off-diagonal Zxy- and Zyx-elements of the impedance tensor rotated to -41° (i.e. 41° counter-clockwise) and the projection of the vertical magnetic transfer function onto the across-strike y-axis (Ty in rotated coordinates).

Because galvanic distortion has an irresolvable scaling effect on the apparent resistivities[39], we concentrated on fitting the impedance phases and the vertical magnetic transfer functions during the inversion. In practice, we only down-weighted the E-Polarization apparent resistivity since 2D modelling can mimic the scaling effect for the B-Polarization. Down-weighting of data subsets is practically achieved by increasing their error bars, which are used to weight the data residuals during the inversion. Here, we imposed a global error floor of 100% on the E-Polarization apparent resistivities, whereas lower error floors of 10% were imposed on the B-Polarisation apparent resistivities. For the impedances phases and for Ty, we employed absolute error floors of 1.5 ° and of 0.03, respectively.

2D Inversion of data with 3D effects may result in biased models or in models that contain phantom structures. Because the E-Polarisation impedance is considered most susceptible to 3D effects[40], some authors prefer to invert only B-Polarisation data or a combination of B-polarization apparent resistivities and phases and vertical magnetic transfer functions[13,41,42]. This approach implicitly corresponds to a rigorous down-weighting of the E-polarization apparent resistivity and phase data with infinite error floors. However, accumulations of charges due to across-strike current flow within a laterally heterogeneous crust may dominate the B-Polarization response even at long periods and mask the response of anomalies within the deeper crust and upper mantle[43]. Therefore,

valuable information about the deeper resistivity structure contained in the E-Polarisation responses could be discarded with this rigorous approach. A heuristic approach to reduce the influence of 3D effects on the inversion result without rejecting these data completely is to down-weight data subsets relative to their departure from pure 2D conditions. Here, we used the ellipticity of the impedance tensor columns to measure the deviation of the data from pure 2D conditions in the presumed strike coordinate system, and adjusted the data errors such that the ellipticities, and hence the departure from 2D conditions, vanish to within the modified errors[26]. We applied this technique to the impedance data at every period and site individually to obtain modified error bars for the entire data set. The error bars of the vertical magnetic transfer function (Ty) were modified accordingly; here we used the absolute value of the off-profile component (Tx) as the error bar on Ty. These modified error bars were used as floor errors, where they exceed the global error floor defined above.

Inverse models were computed with a widely used non-linear conjugate gradient 2D inversion program[30]. The inversion seeks to minimize a Tikhonov regularized functional $\phi = \chi^2 + \tau \mathbf{L} (\log \rho)$ as a trade-off between a structure penalty functional $\tau \mathbf{L} (\log \rho)$ and the sum of the squared data residuals weighted by their variances (χ^2). τ is the trade-off parameter and $\mathbf{L} (\log \rho)$ is a weighted integral of the Laplacian squared of the logarithmic model resistivity ρ.

For the computation of χ^2, lower thresholds for the data errors have been defined in terms of error floors and in terms of errors measuring the departure from the 2D assumption (see above). Statistically estimated data errors (produced with the robust time series processing code) enter the computation of χ^2 only where they exceed the former error measures.

The Laplacian is computed in model domain rather than in space domain, and is thus dependent on the model grid. Effectively, increasing horizontal cell dimensions with increasing distance from the profile support horizontal smoothing, whereas increasing vertical cell dimension with increasing depth result in increased vertical

smoothing. Therefore, we applied weight factors α and β to control the ratio of vertical to horizontal smoothing and to increase horizontal smoothing with increasing depth, respectively. Furthermore, the program allows applying these weight factors to model domains containing cells with dimensions exceeding floor sizes in the horizontal and the vertical directions. For instance, defining the floor size in the vertical direction to correspond to the height of the cells at some depth z_w means that the weight factors α and β become effective only at depths $z>z_w$. We used $\alpha=1$ throughout, and tested β-values between 1 and 3. We found that models computed with $\beta=1$, applied to the entire model domain, and models computed with $\beta=3$, applied only to the model domain deeper than ~20 km, contained very similar structures in the upper ~40 km, but the former appeared vertically stretched at greater depths. Therefore, we used the latter parameter combination.

The trade-off parameter τ, controlling the relative contribution of data residuals and structure penalty to the minimized objective function, was determined from the knee of an L-curve plot, i.e. a cross-plot of data residuals and model norm, here computed for $\tau-$ values between 1 and 1000. The optimal trade-off parameter was found to be close to $\tau = 30$, a value which is typical for the settings being used. We verified our inversion settings by comparing the inversion models with the inversion models produced with the Occam program[44], which inverts simultaneously for resistivity and the regularization parameter. Both inversion programs produced similar results (not shown).

For the inversion, the Pacific Ocean was included as a fixed a priori structure in the starting model. Furthermore, we constrained the parts of the model deeper than 150 km (where sensitivity of our data is poor and lateral resolution is limited by the length of our profiles), to 50 ohm-m to avoid artificial structures appearing at the lower model boundary. Inversion tests confirm that the resistivity of the basal half-space has no significant influence on any of the major features of the inversion models discussed (at depths < 60 km). For the final inversion models shown in this paper, we used these model constraints and the same inversion settings for all seven profiles; only the model grid was adjusted to match varying site distributions along the profiles. In Figures

S2-S8 (Supplementary Information) we depict the observed data, the data predicted by the final inversion models and the data residuals in terms of distance-period pseudosections.

We tested the robustness of structural details contained in the final inversion models with 2D forward modelling and constraint inversion strategies (Figures S3, S6, S7, Supplementary Information), and with 3D forward modelling (Figure S9). Details are provided in the supplementary information.

References

31. Unsworth, M. J., Malin, P., Egbert, G. D. & Booker, J. R., Internal structure of the San Andreas Fault at Parkfield, California. *Geology* **25**, 359-362 (1997).

32. Unsworth, M. J., Bedrosian, P. A., Eisel, M., Egbert, G. D. & Siripunvaraporn W., Along strike variations in the electrical structure of the San Andreas fault at Parkfield, *Geophys. Res. Let.* **27**, 3021-3024 (2000).

33. Egbert, G. D. & Booker, J. R., Robust estimation of geomagnetic transfer functions. *J. R. Geophys. J.* **87**, 173-194 (1986).

34. Ritter, O., Junge, A. & Dawes, G. J. K., New equipment and processing for magnetotelluric remote reference observations. *Geophys. J. Int.* **132**, 535-548 (1998).

35. Weckmann, U., Magunia, A. & Ritter, O. Effective noise separation for magnetotelluric single site data processing using a frequency domain selection scheme. *Geophys. J. Int.* **161**, 456-468 (2005).

36. Egbert, G. D., Robust multiple-station magnetotelluric data processing. *Geophys. J. Int.* **130**, 475-496 (1997).

37. Laakso, T. I. Välimäki, V., Karjalainen, M. and Laine, U. K. Splitting the unit delay—tools for fractional delay filter design," *IEEE Signal Processing Mag.*, **13**, 30–60 (1996).

38. Groom, R. W. and R. C. Bailey. Decomposition of magnetotelluric impedance tensors in the presence of local three-dimensional galvanic distortion, *J. Geophys. Res.* **94**, 1913–1925 (1989).

39. Smith, J. T, Understanding telluric distortion matrices. *Geophys. J. Int.* **122**, 219-226 (1995).

40. Wannamaker, P.E., Affordable Magnetotellurics: Interpretation in Natural Environments, in *Three-Dimensional Electromagnetics*, pp. 349–374, eds Oristaglio, M. & Spies, B., SEG, Tulsa, (1999).

41. Wannamaker, P.E., Jiracek, G.R., Stodt, J.A., Caldwell,T.G., Gonzalez,V.M., McKnight, J.D. & Porter, A.D., Fluid generation and pathways beneath an active compressional orogen, the New Zealand Southern Alps, inferred from Magnetotellurics (MT) data, *J. Geophys. Res.,* **107,** ETG 6, 1–20 (2002).

42. Booker, J.R., Favetto, A. & Pomposiello, M.C., Low electrical resistivity associated with plunging of the Nazca flat slab beneath Argentina, *Nature,* **429,** 399–403 (2005).

43. Becken, M., Ritter, O., & Burkhardt, H., Mode separation of magnetotelluric responses in three-dimensional environments. *Geophys. J. Int.* **172**, 67-86 (2008a).

44. deGroot-Hedlin, C. & S. Constable, Occam's inversion to generate smooth two-dimensional models from magnetotelluric data, *Geophysics* **55,** 1613–1624 (1990).